

MICROBIOLOGY

Cell-autonomous diversification in bacteria arises from calcium dynamics self-organizing at a critical point

Christian T. Meyer and Joel M. Kralj*

How dynamic bacterial calcium is regulated, with kinetics faster than typical mechanisms of cellular adaptation, is unknown. We discover bacterial calcium fluctuations are temporal-fractals resulting from a property known as self-organized criticality (SOC). SOC processes are poised at a phase transition separating ordered and chaotic dynamical regimes and are observed in many natural and anthropogenic systems. SOC in bacterial calcium emerges due to calcium channel coupling mediated via membrane voltage. Environmental or genetic perturbations modify calcium dynamics and the critical exponent suggesting a continuum of critical attractors. Moving along this continuum alters the collective information capacity of bacterial populations. We find that the stochastic transition from motile to sessile lifestyle is partially mediated by SOC-governed calcium fluctuations through the regulation of c-di-GMP. In summary, bacteria co-opt the physics of phase transitions to maintain dynamic calcium equilibrium, and this enables cell-autonomous population diversification during surface colonization by leveraging the stochasticity inherent at a boundary between phases.

Copyright © 2023 The Authors, some rights reserved; exclusive licensee American Association for the Advancement of Science. No claim to original U.S. Government Works. Distributed under a Creative Commons Attribution NonCommercial License 4.0 (CC BY-NC).

INTRODUCTION

Compared to eukaryotic systems, little is understood regarding how bacteria manage ion flux (1–4). Because of their size, small ionic changes are sufficient to drastically alter bacterial electrophysiology (3). In the case of free Ca^{2+} , bacteria must balance an external concentration of up to 1 mM against an internal concentration as low as 300 nM (5). As was noted by Benarroch and Asally (3), the small size of a bacterium is consequential for its electrophysiology. For a femtoliter cell with a membrane capacitance of $1 \mu\text{F}/\text{cm}^2$, a surface area of $6 \mu\text{m}^2$, and an internal Ca^{2+} concentration of 300 nM (5), the addition of a mere 180 free Ca^{2+} ions to the cytoplasm would double the molar concentration and increase the membrane potential by 1 mV ($V_m = q/C$ where $q = 180 \times 1.6 \times 10^{-19}$ Coulombs/proton and $C = 1 \mu\text{F}/\text{cm}^2 \times 6 \times 10^{-8} \text{ cm}^2$). The kinetics of Ca^{2+} fluctuations are much faster ($\sim\text{ms}$) (6) than typical mechanisms of biological adaptation such as transcription and posttranslational modifications. Yet, despite these kinetic challenges, bacteria use dynamic Ca^{2+} in numerous processes including motility, energy production, and virulence (2, 3, 7). How is this dynamic equilibrium maintained without enormous energy loss to continuously coordinate ion flux? Here, we find evidence that Ca^{2+} flux is governed by the physics of phase transitions, specifically a transition between dynamical regimes in a process termed self-organized criticality (SOC) (8).

SOC has been studied in a wide range of seemingly disparate phenomena ranging from flocking birds to ferromagnets to the architecture of the brain (9–16). Rather than separating states of matter, SOC systems are characterized by the separation of dynamical regimes, colloquially termed “order at the edge of chaos” (17). The classic example of SOC is sand falling and forming into a pile; as sand continues to fall, the pile alternates between avalanches and growth (8). While the avalanches’ timing is stochastic, the statistical relationship between its size and duration is predictable. All SOC systems have universal properties permitting their collective

behavior to be described with statistical models while neglecting the intricacies of the system’s subcomponents. For example, the size and duration of avalanches in a SOC system have probability distributions well described by a power law (9, 17). Power-law scaling leads to scale invariance whereby the statistical behaviors of these systems do not depend on the size of the spatial or temporal domain (i.e., changing the size of the sand pile does not alter the relationship between avalanche size and duration) (9, 17).

Here, we investigate whether SOC governs Ca^{2+} flux within a single-celled bacterium. This inquiry was prompted by the observation of anomalous structures in the power spectra of a Ca^{2+} sensor expressed in *Escherichia coli* when characterizing the type of noise in bacterial Ca^{2+} regulation.

RESULTS

Fluctuations in bacterial Ca^{2+} are scale-free

We previously reported mechanically-stimulated, voltage-gated Ca^{2+} flux in individual *E. coli* (6). We were curious how the Ca^{2+} dynamics were distributed within a large population of bacteria. Therefore, we imaged hundreds of bacteria expressing GCaMP6f (18) mechanically stimulated via immobilization under an agarose pad (Fig. 1A). GCaMP6f is optimally sensitive in the range of measured cytosolic Ca^{2+} concentration in *E. coli* [300 to 1000 nM; (5)] saturating above 10 μM . Initial experiments imaged Ca^{2+} fluctuations at a 200-ms interval (5 Hz; Fig. 1B). We were surprised that the fluctuation amplitude increased as imaging frequency decreased down to 0.05 Hz (every 20 s; Fig. 1C). However, after rescaling, the traces appeared self-similar and became visually indistinguishable (fig. S1 and movie S1). In contrast, the fluctuation amplitude in a Ca^{2+} -insensitive, fluorescent protein (mScarlet) expressed from the same promoter did not depend on the imaging frequency (Fig. 1D). This suggested that Ca^{2+} fluctuations were scale-free (Table 1). Scale-free processes appear self-similar with rescaling when measured at different temporal scales and are characteristic of many natural and anthropogenic processes exhibiting fractal dynamics (9, 19, 20).

BioFrontiers and MCDB Department, University of Colorado Boulder, Boulder, CO, 80303, USA.

*Corresponding author. Email: joel.kralj@colorado.edu

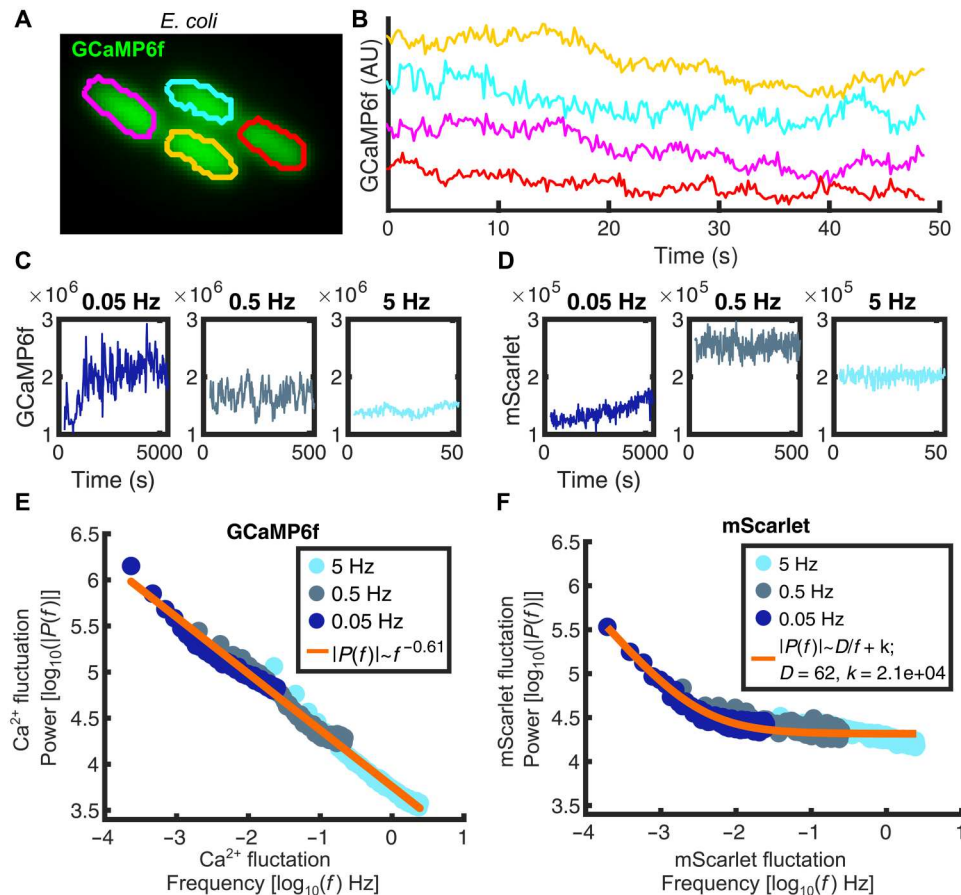


Fig. 1. Ca²⁺ fluctuations in bacteria are temporal fractals. (A) *E. coli* imaged via GCaMP6f fluorescence. Segmentation mask overlaid (see Materials and Methods for segmentation algorithm). (B) Extracted GCaMP6f traces from the segmentation mask in (A). Images were taken every 200 ms (5 Hz). The first 15 frames of each trace are removed before analysis due to initial photobleaching. Colors correspond to outlines in (A). (C) Raw GCaMP6f signal in an *E. coli* cell imaged at 0.05 Hz (left), 0.5 Hz (middle), and 5 Hz (right). Each panel is a different cell. (D) mScarlet signal imaged at the same frequencies. mScarlet is expressed from the same promoter as GCaMP6f. (E) One-sided power spectrum of GCaMP6f traces at different imaging frequencies (points, blue; gray, cyan). The x axis corresponds to the Ca²⁺ fluctuation frequency, and the y axis corresponds to the Ca²⁺ fluctuation power. Cell totals for each condition are 1665, 1538, and 2816 for 0.05, 0.5, and 5 Hz, respectively. The power-law exponent is calculated by linear regression on a log-log plot (orange line). (F) Power spectrum for mScarlet expressed from the same promoter. Cell totals for each condition are 3320, 5954, and 9485 for 0.05, 0.5, and 5 Hz, respectively. Flicker noise equation fit calculated by nonlinear regression (orange line). See fig. S2F for comparison of different model fits of the mScarlet and GCaMP6f signals. AU, arbitrary units.

To test Ca²⁺ dynamics for scale invariance, the one-sided power spectrum (Table 1) was calculated for both GCaMP6f and mScarlet signals. The GCaMP6f power spectrum showed that Ca²⁺ fluctuations were scale-invariant characterized by power-law scaling (Fig. 1E and Table 1) with the appropriate collapse when the traces were normalized (fig. S2A). In contrast, the mScarlet power spectrum was better fit by an equation for flicker noise—a noise characteristic of camera shot noise (21) containing 1/f noise at low frequencies and white noise at high frequencies (Fig. 1F). Unlike the GCaMP6f signal, the mScarlet spectra did not collapse when normalized (fig. S2B). This verified that the fractal dynamics were not a result of promoter expression (22). Heat killed *E. coli* maintained GCaMP6f fluorescence, but the scale invariant dynamics were abolished (fig. S2C), indicating that active metabolism was required and that the power spectra are not a result of fluorescent depletion or quenching effects of GCaMP6f. Scale invariance was also not observed for fluorescein, a cell-free dye excited by the same laser as GCaMP6f (fig. S2D). These data verified that the

fractal dynamics in the GCaMP6f signal were intrinsic to living cells and were not a result of camera, laser, or chemical noise. Scale invariance for GCaMP6f was also observed on a different optical system (fig. S2E).

To quantify the validity of the selected fits for each spectrum, we calculated the likelihood of a power-law, exponential, or flicker noise function using the Akaike Information Criterion (AIC; Table 1). We found that a power law was more likely (lower AIC) than exponential or flicker noise functions in fitting the GCaMP6f power spectra (fig. S2F, blue versus red and yellow bars). In contrast, the flicker noise function was more likely for the mScarlet power spectra (fig. S2F) as well as the heat killed and fluorescein controls (fig. S2G). Further evidence of scale invariant bacterial Ca²⁺ dynamics was observed when we examined the Hurst exponent (fig. S3 and Table 1) and autocorrelation function (ACF; fig. S4 and Table 1) of the GCaMP6f signal. Both the Hurst exponent and ACF are measures of long-term memory in a time series—a characteristic of scale free processes. The ACF and power spectra also ruled out

Definitions	
Ca ²⁺ trace	The abundance of free Ca ²⁺ ions in a single bacterial cell over time measured using the fluorescent GCaMP6f reporter.
Imaging frequency	Measured in Hz, this is the inverse of the imaging interval. A 5-Hz frequency corresponds to an image taken every 200 ms.
Imaging exposure	Measured in ms, this is the duration of simultaneous sample illumination and photon capture.
Scale free	A scale free process has statistical properties which are invariant to the time/spatial domain size. Synonymous with scale invariant.
Power law	A function of the form $F \sim x^{-k}$ where k is the power-law exponent. When a probability distribution follows a power law, large events are more common than for a random process ($F \sim e^{-x}$).
Power spectra	Computed using a Fourier transform, power spectra show the relationship between the signal variance and frequency. For fluorescence signal, the signal variance has units of [AU] ² /Hz.
Temporal fractal	Temporal fractals are time series signals that are scale free appearing self-similar as the temporal domain changes.
ACF	Correlation of a signal with a phase shifted copy of itself as a function of the phase shift.
AIC	An information theory–based metric to measure the relative likelihoods of different model fits accounting for model complexity.
OU	Stochastic model of an overdamped spring with friction.
Critical point	A phase transition in which the system develops semi-ordered dynamics and properties such as universality.
SOC	A system with an attractor at a critical point.
Attractor	A low-energy state of a system toward which the system will evolve according to the second law of thermodynamics.
Branching analysis	A method to detect critical dynamics in a system developed by Larremore <i>et al.</i> (27). See Fig. 2A.
Critical exponent	A universal value describing the statistical properties of systems at a critical point.
Mean size scaling	Method of calculating the critical exponent $1/\sigma\mu z$ by fitting a power law to the average size of an avalanche as a function of its duration.
Avalanche collapse	Method of calculating the critical exponent $1/\sigma\mu z$ by observing how avalanches of different periods collapse onto the same curve when renormalized by the critical exponent.
Crackling noise	Method of calculating the critical exponent $1/\sigma\mu z$ based on the power-law exponents of the probability distributions for the avalanche duration and size.
Frobenius eigenvalue	The maximum eigenvalue of a matrix. Denotes the dominant mode of a system of interacting components over time.

continued on next column

Definitions	
Perron-Frobenius theorem	The Frobenius eigenvalue of a matrix is bounded by the minimum and maximum sum of the matrix rows for a positive definite matrix.
Ohm's law	Relationship between a circuit's voltage, current, and conductance.
Entropy	A measure of the uncertainty of a variable based on Shannon's information theory.
MI	From information theory, MI measures the information known about one variable given another variable.
Sessile growth	Microbial growth while attached to a solid substrate.
FRET sensor	Two fluorophores connected by a linker which changes conformation upon binding the target molecule resulting in FRET signal between the fluorophore pairs.
PDE (bacteria)	Class of enzymes responsible for reducing c-di-GMP pools by linearizing c-di-GMP to pGpG.
c-di-GMP	Used as a secondary messenger, the accumulation of this cyclic di-nucleotide results in transcriptional programs for sessile growth and biofilm formation.

Symbols	
h	Hurst exponent. Related to the fractal dimension of a temporal signal.
Λ	Branching ratio. Equal to a signal divided by a phase shifted copy of itself.
S	Avalanche size equal to the integrated fluorescence signal. See Fig. 2D.
T	Avalanche duration in number of frames. See Fig. 2D.
α	Power-law exponent describing the avalanche size (S) probability distribution.
τ	Power-law exponent describing the avalanche duration (T) probability distribution.
$1/\sigma\mu z$	Universal critical exponent which can be calculated several ways. If a system is well described by SOC, then the different methods of calculating this exponent will agree (9, 13, 30).
A	Matrix of interaction strengths between nodes (channels) in the network model.
λ	Maximum (Frobenius) eigenvalue of the interaction matrix A . Determines the long-term behavior of this system. When $\lambda = 1$ the system is at a critical point.
Φ	Calcium flux (i.e., current) in the ODE model.
Σ	Proportion of open channels at any time step.
ρ	Maximal conductance assuming all Ca ²⁺ channels are open.
V_m	Voltage across the membrane.
P_r	Pumping rate of Ca ²⁺ pumps in model.
$H(S)$	Entropy of avalanche sizes according to Shannon information theory.

Downloaded from https://www.science.org on April 09, 2025

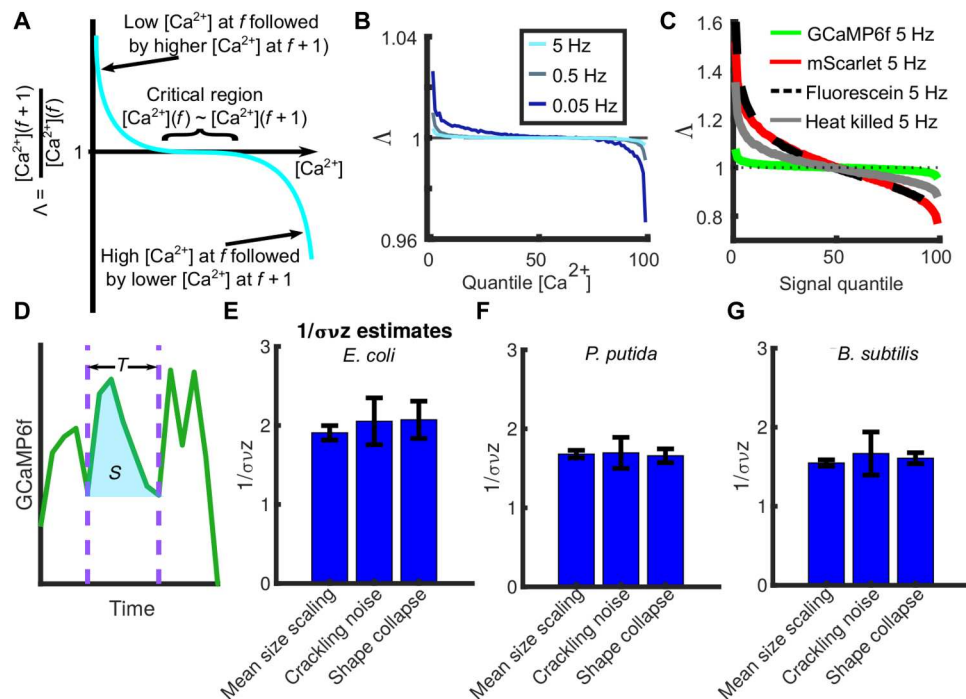


Fig. 2. Ca^{2+} dynamics in bacteria exhibit the hallmarks of SOC. (A) Branching analysis. For a critical process, the branching function Λ shows a characteristic sigmoid shape. For high values of $[\text{Ca}^{2+}]$ at frame f , the expected value at $f + 1$ is smaller as the system is driven back to equilibrium. Conversely, for low values of $[\text{Ca}^{2+}]$ at f , the expected value at $f + 1$ is higher. The breadth of the critical region relates to the stability of the critical dynamics. (B) Plotted is the mean value of the branching ratio (Λ) for each quantile of GCaMP6f signal for three different imaging frequencies (legend). As the sampling frequency decreases, the amplitude of Λ at the edges increases as expected for a process with power-law scaling (Fig. 1E). (C) The branching ratio for noncritical controls. All conditions were measured at the same imaging frequency. (D) Definition of a Ca^{2+} avalanche. For each cell, the GCaMP6f trace is divided into domains between two changes in the sign of the derivative (purple dotted lines). The period (T) of each avalanche is the discrete number of frames within each domain (black arrows), and the size (S) is the signal integral within the domain (blue overlay). (E) Bar plot of the three different estimates of the critical exponent $1/\text{ovz}$. Avalanches from three replicates were bootstrap resampled 100 times with replacement to estimate the SD in the three estimates (black error bars). See fig. S5 for individual calculations. (F) Estimates of $1/\text{ovz}$ for *P. putida*. (G) Estimates of $1/\text{ovz}$ for *B. subtilis*. See fig. S8 for individual calculations.

the possibility that the power law could be trivially explained by an Ornstein-Uhlenbeck process (fig. S4 and Table 1) (23, 24).

In summary, we found that cytosolic fluctuations in bacterial Ca^{2+} under mechanical stimulation were temporal fractals (Table 1) exhibiting self-similar dynamics across multiple time scales. Scale-free processes are a common solution for biological systems that need to maximize dynamic range in unpredictable environments and encode memory via long-term autocorrelations (25, 26).

SOC governs dynamic equilibrium in bacterial Ca^{2+}

Temporal fractals are frequently observed in systems poised at a transition between ordered and chaotic dynamics. This boundary between dynamical regimes is well described by the mathematics of phase transitions, and the point separating the two regimes is called the critical point (Table 1) (9). An illustrative example of this type of phase transition are neural circuits where the critical point is defined by the coupling strength between neurons (27, 28), and the brain is homeostatically set to a coupling strength at a critical point that maintains dynamic equilibrium in neural activity (29). Therefore, we hypothesized that bacterial Ca^{2+} flux is poised at a critical point, being neither completely chaotic nor highly ordered, giving rise to the scale-invariant dynamics observed in Fig. 1.

We used branching analysis to detect criticality (Table 1) (27). The branching ratio (Λ) is defined as the ratio between the Ca^{2+} signal at frame f and the next frame $f + 1$. The signature of a critical process is a wide domain over which Λ is equal to 1 with characteristic sigmoid tails (Fig. 2A). The sigmoid tails indicate a nonlinear restorative force which reduces Ca^{2+} at $f + 1$ when Ca^{2+} is high at frame f (right side) and vice versa (left side). Λ , calculated from the GCaMP6f traces, showed clear evidence of criticality with appropriate scaling for a scale-free process between sampling frequencies (Fig. 2B). In contrast, the mScarlet, fluorescein, and heat-killed controls are less flat than the GCaMP6f branching ratio at matching imaging frequencies (Fig. 2C). Therefore, the branching analysis indicated a strong nonlinear restoring force in maintaining Ca^{2+} flux in bacteria but with a wide range of stable values—a hallmark of a critical point.

We further hypothesized that this critical point was self-organized. SOC (Table 1) systems are defined by having the critical point as an attractor (Table 1); the systems' dynamics drive it toward the critical point. SOC systems are predicted to have additional statistical properties including power-law relationships in the size, shape, and duration of the fluctuations at the critical point (9, 30). Therefore, we tested whether the Ca^{2+} dynamics were described by SOC. An "avalanche" is required for SOC analyses. We defined a Ca^{2+} avalanche as the domain between two changes in the sign of

the derivative of the GCaMP6f signal (Fig. 2D). Within this domain, each avalanche has an integrated size (S) and duration (T). We note that the avalanche construct was necessitated to investigate our system using classic SOC analysis frameworks (see the “Limitations of study” section). We interpreted these Ca^{2+} avalanches as cascades of channels opening followed by efflux via ion pumps before the channels open again. To test whether the Ca^{2+} dynamics were well described by SOC, we examined three ways of calculating the universal critical exponent $1/\sigma_{\text{vz}}$ (see Table 1 and Materials and Methods) (13, 31). The critical exponent $1/\sigma_{\text{vz}}$ describes the scale invariant properties of a SOC process. Presently, the most rigorous test for identifying a SOC process is to calculate $1/\sigma_{\text{vz}}$ three different ways (13, 30). Estimates of $1/\sigma_{\text{vz}}$ from these three different approaches will agree for a SOC system.

1) Mean size scaling. The first estimate of $1/\sigma_{\text{vz}}$ was determined by fitting the scaling exponent relating the mean avalanche size to the avalanche duration [$\langle S(T) \rangle \sim T^{1/\sigma_{\text{vz}}}$]. As predicted for a SOC system, the mean Ca^{2+} avalanche size scales by the duration according to a power law (fig. S5A). The power-law exponent equaled $1/\sigma_{\text{vz}} = 1.91 \pm 0.09$.

2) Crackling noise relationship. The second estimate was calculated from the “crackling noise” relationship between the power-law exponents for the probability distributions of S and T (τ and α , respectively) (9, 30). We found that the probability density function of S was a power law as determined by the Kolmogorov–Smirnov (KS) test algorithm proposed by Clauset *et al.* (32) ($D = 0.00821$, $P = 0.84$; fig. S5B). Examining the probability distribution of the duration (T), we found it necessary to use a moving mean smoothing function to account for microscope noise breaking up longer avalanches but found that the T also is fit by a power law ($D = 0.0627$, $P = 0.8$; fig. S5C). Power-law exponents were $\tau = 2.86$ and $\alpha = 4.82$, respectively, leading to a crackling noise estimate of $(\alpha - 1)/(\tau - 1) = 1/\sigma_{\text{vz}} = 2.09 \pm 0.27$. We note that this method of calculating $1/\sigma_{\text{vz}}$ was the least robust due to the sensitivity of the α exponent to the data preprocessing.

3) Avalanche shape collapse. The third estimate was calculated from the shape collapse algorithm, which stipulates that all the avalanches from different periods should collapse onto the same curve when rescaled by $(1 - 1/\sigma_{\text{vz}})$. We fit this scaling exponent by minimizing the variance between renormalized, mean avalanche shapes for all periods (T) as previously proposed in (31) using a custom MATLAB implementation. On the basis of the shape collapse algorithm, $1/\sigma_{\text{vz}} = 2.07 \pm 0.21$ (fig. S5D).

The agreement between the three estimates of the critical exponent (Fig. 2E) demonstrated that Ca^{2+} maintenance was indeed SOC in *E. coli* according to the most rigorous proposed method. Changing the definition of an avalanche to periods when the signal exceeded a static threshold resulted in the same correspondence between the three approaches scaling estimates of $1/\sigma_{\text{vz}}$ (fig. S6). Consistent with our observation that Ca^{2+} fluctuations were scale-free, the mean size scaling estimate of $1/\sigma_{\text{vz}}$ did not depend on the sampling frequency (fig. S7). Ca^{2+} dynamics of other bacterial species (*Pseudomonas putida* and *Bacillus subtilis*) also exhibited SOC (Fig. 2, F and G, and fig. S8). We note that the T distribution for *B. subtilis* did not pass the stringent KS test in (32) for a power law; nevertheless, the most likely α still resulted in a crackling noise estimate of $1/\sigma_{\text{vz}}$ that was similar to the mean scaling and avalanche collapse estimates (Fig. 2G).

Therefore, our data indicated dynamic Ca^{2+} homeostasis was maintained by SOC in diverse single-cell organisms. SOC resolves the tension between coordinating dynamic activity while preserving long-term stability by leveraging the statistical properties of critical points.

Ising-like model of Ca^{2+} regulation recapitulates key features of SOC

We were next interested in the minimal components required for recreating SOC in Ca^{2+} maintenance. We assumed that Ca^{2+} influx is regulated by Ca^{2+} channels and efflux is regulated by Ca^{2+} pumps. Because the biophysical characteristics and identity of the *E. coli* Ca^{2+} channels and pumps remain unknown (33), we pursued an abstract, Ising-like model (Fig. 3, A and B). Ising models are common models to study SOC processes (9) and are composed of interacting species (nodes in a network) with a coupling strength (edges in a network) at a critical point. Our modeling approach adapted Ising-like models of SOC dynamics in neural systems which have previously been found to be predictive of the statistical distributions of neuronal avalanches observed in vivo (27, 34). In our model, the probability of any one Ca^{2+} channel opening depends on the sum of all its neighbor's states times their relative interaction strength (Fig. 3B). If the channels are too strongly coupled, then when one channel opens, they all open (Fig. 3C). If the channels are too weakly coupled, then they all eventually close. Spontaneous and ceaseless dynamics are only achieved if the coupling strength is right at the critical point. Mathematically, we measure the proximity to this critical point by the maximum eigenvalue (λ ; Table 1) of the interaction matrix (A). The maximum eigenvalue has previously been shown to determine the long-term behavior of a system (Fig. 3C) (27, 34, 35). For a control model, we set the coupling strength to zero and randomly open and close each channel with a 50% probability at each time step. We note that the magnitude of the noise in the random model depends on the number of channels simulated (fig. S9, B to E), but the statistics of the noise (e.g., branching ratio, ACF, and power spectra) will retain the same characteristics.

Building on the Ising model of coupled Ca^{2+} channels, we added a Hodgkin-Huxley model of voltage-driven ion flux to simulate how Ca^{2+} fluctuations would depend on the biophysical characteristics of, at present, unknown Ca^{2+} channels and pumps. In both the SOC and random model, the Ca^{2+} influx through the channels was driven by electrodiffusion, based on Ohm's law ($I = V \cdot G$) where I is the current, V is the voltage, and G is the conductance (Fig. 3A, purple, and Table 1). We use the Hodgkin-Huxley approximation whereby V is equal to the difference between the membrane voltage (V_m) and the reversal voltage, equal to the log of the ratio of external and internal Ca^{2+} (also called the Nernst potential) (I). The conductance was determined by the percentage of open channels (Σ) times the maximal conductance (ρ). Ca^{2+} efflux was driven by deterministic pumps (Fig. 3A, blue) with a rate (P_r). The models' full derivation and assumptions are detailed in Materials and Methods and the Supplementary Materials. Additional model limitations are discussed in the “Limitations of study” section. Visual inspection of simulation traces for the two models revealed that the SOC-coupled model had a larger dynamic range than the random model for the same number of channels (Fig. 3D).

To assess the model's performance, we investigated how it matched four experimental observations (Table 2): (i) power-law

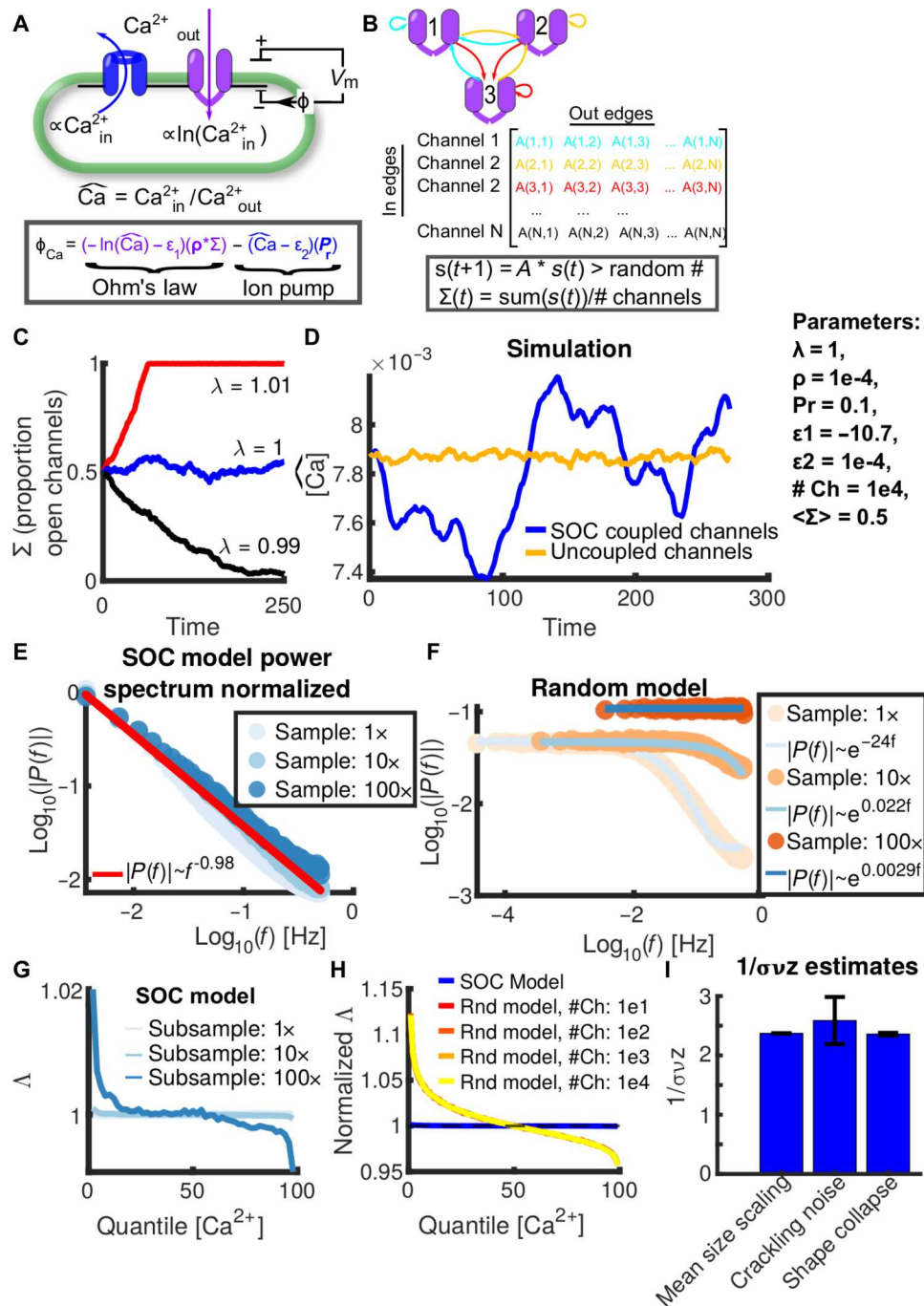


Fig. 3. Coupling between Ca^{2+} channels was poised at a critical point within a bacterium. (A) Schematic of an ODE model of Ca^{2+} flux. The influx is determined by Ca^{2+} channels (purple) according to Ohm's law. Efflux is governed by an ion pump (blue) with a pump rate (P_r). (B) Cartoon of the channel network. Each channel (node) interacts with every other channel (arrows). The strength of these interactions defines a matrix (A). The rows correspond to the in edges and the columns to the out edges. The state vector (S) at time $t + 1$ is determined by the sum of all channels' current state (0,1) at time t multiplied by the weight of each interaction (A). See fig. S9A for distribution of edge weights in A . Σ is equal to the proportion of open channels at any given time. (C) Σ for coupled simulations when the maximum eigenvalue (λ) of A is equal to 1.01 (red), 1 (blue), and 0.99 (black). (D) Example simulation traces for random-uncoupled (gold) and SOC-coupled (blue) channels. The average probability of opening in both cases is 50%. The simulation time step is arbitrary and therefore unitless. (E and F) The normalized power spectra from simulations for SOC coupled model (E) and uncoupled channels model (F) at different subsampling frequencies. SOC model power spectra fit with a power law while the random model fit with an exponential function. See fig. S9 (F and G) for AIC calculations. (G) Branching analysis for different subsamples of the SOC model. (H) Comparing the branching ratio for the random model with different numbers of channels and the SOC model (blue). (I) Bar chart of the critical exponent for the simulated model based on the three methods of calculation. See fig. S9 (K to N) for individual calculations. The error bars were determined by bootstrap resampling 100 times with replacement.

Table 2. Model predictions matching experimental results.		
	Model predictions	Experimental results
Power spectra of SOC-governed Ca ²⁺ fluctuations	Fig. 3E and fig. S9, F and G	Fig. 1E and fig. S2, A and F
Branching ratio of Ca ²⁺ fluctuations	Fig. 3G	Fig. 2B
Autocorrelation function of Ca ²⁺ signal	fig. S9, I and J	fig. S4A
Hallmarks of SOC	Fig. 3I and fig. S9, K to N	Fig. 2, E to G, and fig. S5
Entropy as a function of the critical exponent 1/σ _μ z	Fig. 5D	Fig. 5E

fit of power spectra, (ii) shape of branching ratio, (iii) shape of auto correlation function, and (iv) agreement of critical exponent calculations for a SOC process.

1) As with our experimental data, the power spectra of Ca²⁺ traces generated by the SOC model was best fit by a power law, invariant to subsampling which collapsed when normalized (Fig. 3E and fig. S9F). This behavior matched the power spectra for the GCaMP6f signal. In contrast, the random model’s power spectra were better characterized by an exponential function fit (Fig. 3F and fig. S9G). In this way, the random model does not capture the noise profile of the experimental controls (e.g., mScarlet or heat killed GCaMP6f) which were better fit by a flicker model. This indicated that the noise profile of the random model and the experimental controls collected by optical imaging are different.

2) The branching ratio (Λ) for the SOC model had the same shape as the experimental data as well as the experimentally observed scaling as a function of subsampling the model simulations (Fig. 3G and fig. S9H). In contrast, the Λ for the random model was less “flat” as it lacked the nonlinear restoring force (i.e., memory) of the SOC model—a characteristic that was invariant to increasing the magnitude of the random model’s noise by reducing the number of channels (Fig. 3H).

3) The ACF of the SOC model matched the experimental data, while the random model had no autocorrelations irrespective of the magnitude of the noise (fig. S9I). In addition, the ACF was the same for subsampled traces of the model (fig. S9, I and J).

4) The SOC-coupled model had a critical exponent with the hallmarks of SOC (Fig. 3I and fig. S9, K to N) in concordance with the experimental data.

The invariance of the branching ratio, power spectrum, and ACF statistics in the SOC model to different time steps confirmed that an arbitrary time step is acceptable for modeling a scale-invariant process as was assumed in (27). Despite its simplicity, our model reproduced numerous aspects of our experimental data and suggests that the scale invariance emerges due to coupling between yet unidentified Ca²⁺ channels.

Voltage is the mechanism by which the Ca²⁺ channels are coupled

We hypothesized that the coupling between the Ca²⁺ channels was mediated either by membrane voltage or a diffusible factor. In

support of voltage-mediated coupling, the branching function was less flat, and scale invariance was destroyed when membrane voltage was dissipated using the protonophore carbonyl cyanide *m*-chlorophenyl hydrazone (CCCP) at pH 8.2 (Fig. 4, A and B, and fig. S10). At this pH, all the proton motive force is carried by the membrane voltage. Although scale invariance was destroyed, viability was maintained (fig. S11). This led us to conclude that CCCP does not induce super- or sub-critical dynamics (i.e., λ > 1 or λ < 1) but rather increases the number of random acting channels by decoupling them, hence the cells remain viable but with a smaller dynamic range in Ca²⁺ fluctuations as predicted in the model (Fig. 3D). In addition, this result further demonstrates that the power law in the power spectra of GCaMP6f are not a result of fluorophore-specific chemical properties.

To further test whether voltage mediated the coupling between Ca²⁺ channels, we created bacterial “cables” by treating *E. coli* cells with cephalixin which inhibits late-stage bacterial segmentation. Imaging a 61.8-μm cell at 214 Hz, we attained a temporal resolution of 5 ms per frame (movie S2 and Fig. 4C). In 5 ms, the mean passive diffusion lengths for an adenosine triphosphate (ATP) molecule, a Ca²⁺ ion, and a proton are 1.8, 2.3, and 7.8 μm, respectively (Fig. 4C, scale bars; see Materials and Methods). Partitioning the cell into 11 segments of 5.6 μm in length, we find the influx of Ca²⁺ to occur simultaneously across all segments (Fig. 4, D and E). Fitting a convolution to GCaMP6 traces from single pixels, we found that coordinated Ca²⁺ influx was simultaneous to within 4.6 ms across the entire cell (Fig. 4F and see Materials and Methods). Examining two other cells of shorter length, we found the same simultaneous Ca²⁺ flux across the length of the cell (fig. S12, A to H). One of the cells exhibits stacking peaks in the GCaMP6f signal demonstrating that the avalanches need not be temporally separated. These kinds of overlapping avalanches were also observed in other SOC systems such as neural circuits. Therefore, passive transport within the cytoplasm could not explain the spatial coordination of Ca²⁺ influx.

We interpret these inflection points as the phase transitions of Ca²⁺ channels in the cell, while the signal decay is driven by the efflux from Ca²⁺ pumps and photobleaching due to the high laser power used to image above 200 Hz. Because of the difficult nature of collecting these images, we were limited to examining approximately 30 cells of which only 3 had a Ca²⁺ avalanche large enough to register above the signal noise during imaging. As indicated by the power spectrum (Fig. 1E), the magnitude of the Ca²⁺ fluctuations decreased as the imaging frequency increased. Therefore, we would expect fewer avalanches of sufficient size to detect optically when imaging over 200 Hz as done for these movies.

On the basis of our theory of voltage coupling, we predicted that if we uncoupled the channels by setting the membrane voltage to zero, then we would lose this spatial coordination in flux. To test this, we ran a similar experiment but in addition to treating the bacteria with cephalixin, we also treated them with CCCP (100 μM). In the absence of membrane voltage, we found that Ca²⁺ is no longer coordinated across the cell. This can be observed in the presence of discrete areas with a greater time delay (red- > yellow; fig. S12, I to L). However, one limitation of this observation is that the size of the CCCP-treated Ca²⁺ flux is smaller, as predicted by the model, and therefore more sensitive to noise in the convolution. Nevertheless, in combination with the evidence of the branching analysis and power spectrum for the CCCP-treated cells as well the spatial coordination faster than a proton can diffuse, we conclude that voltage is

Downloaded from https://www.science.org on April 09, 2025

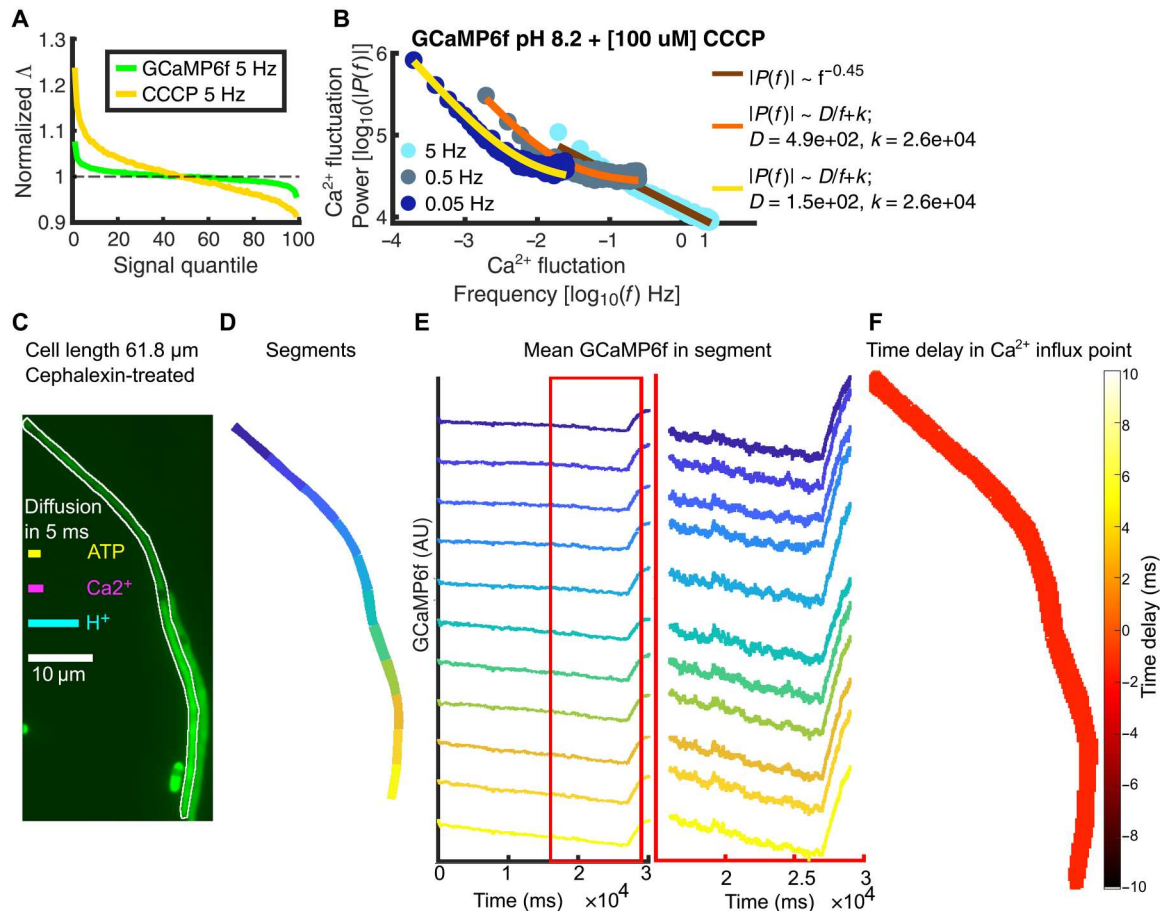


Fig. 4. Ca^{2+} influx is coordinated by membrane voltage. (A) Comparing the branching function of the GCaMP6f signal for cells treated with the ionophore CCCP (100 μM at pH 8.2) (yellow) to untreated cells (green). Cells were treated for 1 hour before plating on the pad containing matching concentration of CCCP and imaged. (B) Normalized power spectra of Ca^{2+} flux when cells are treated with CCCP at three imaging frequencies. See Fig. S10 for AIC calculations. (C) A cephalexin-treated *E. coli* cell expressing GCaMP6f was imaged at 214 Hz (4.67-ms sampling) for 30 s (see movie S2). White boundary marks manual segmentation. Diffusion length for ATP (yellow), Ca^{2+} (magenta), and H^+ (cyan) over 5 ms depicted. See Supplementary Methods for calculation details. (D) Cell was partitioned into 11 5.6- μm segments (colormap). (E) The left shows the mean GCaMP6f signal over time within each segment over the 30-s experiment. The right shows an expanded 2-s window around the inflection point (orange outline, left). (F) The pixel-wise time delay in the Ca^{2+} influx (colormap) compared to the whole-cell mean (see Supplementary Methods). The lack of spatial organization in the time delay along the growth axis indicates that the coordination is faster than the imaging rate.

the most likely agent coupling the Ca^{2+} channels. This coupling, poised at a critical point, was necessary for scale-invariant dynamics to emerge in the model.

The collective information processing of bacteria depends on the critical exponent

Using the SOC model, we attempted to predict the impact of changing the channel conductance (ρ) or the pumping rate (P_r) on the critical exponent ($1/\sigma\nu z$). We reasoned that these parameters could be altered both by cell-intrinsic and cell-extrinsic factors. Increases in P_r decreased $1/\sigma\nu z$, while changing ρ had a more modest impact over the range of values tested (Fig. 5A). Changes in ρ and P_r led to smoothing the Ca^{2+} dynamics (Fig. 5B) while maintaining criticality ($\lambda = 1$). Therefore, our model predicts that the confluence of genetic and environmental factors alters the critical exponent by modifying ρ and P_r . In experiments, we observed five classes of perturbations that experimentally modified the critical exponent:

mechanical stiffness, environmental pH/osmolarity, antibiotic stress, nutrient availability, and metabolic mutants (Fig. 5C).

Changing the mechanical environment by adhering with poly-L-lysine resulted in a modest decrease in the critical exponent when compared to cells adhered with agarose in either PMM or M9 media (Fig. 5C, cyan and salmon bars). Reducing the pH to 6.5 reduced the critical exponent, while increasing the pH to 8.5 increased the exponent (Fig. 5C, blue bars). The largest impact on the critical exponent was the knockout $\Delta btuR$ involved in vitamin B12 synthesis and previously identified to modify Ca^{2+} dynamics from a genome-wide screen (33). The absence of amino acids (PMM versus M9 media) or substituting arabinose for glucose as a carbon source also increased the exponent (Fig. 5C). This suggested that $1/\sigma\nu z$ depended on the metabolic profile of the cell. In support of this, knocking out components in F1Fo-ATP synthase (atp) or the reduced form of nicotinamide adenine dinucleotide oxidoreductase (nuo) also altered the critical exponent. Specifically, knockouts that result in a non-functional F1Fo complex ($\Delta atpE$ and $\Delta atpC$) decreased the critical

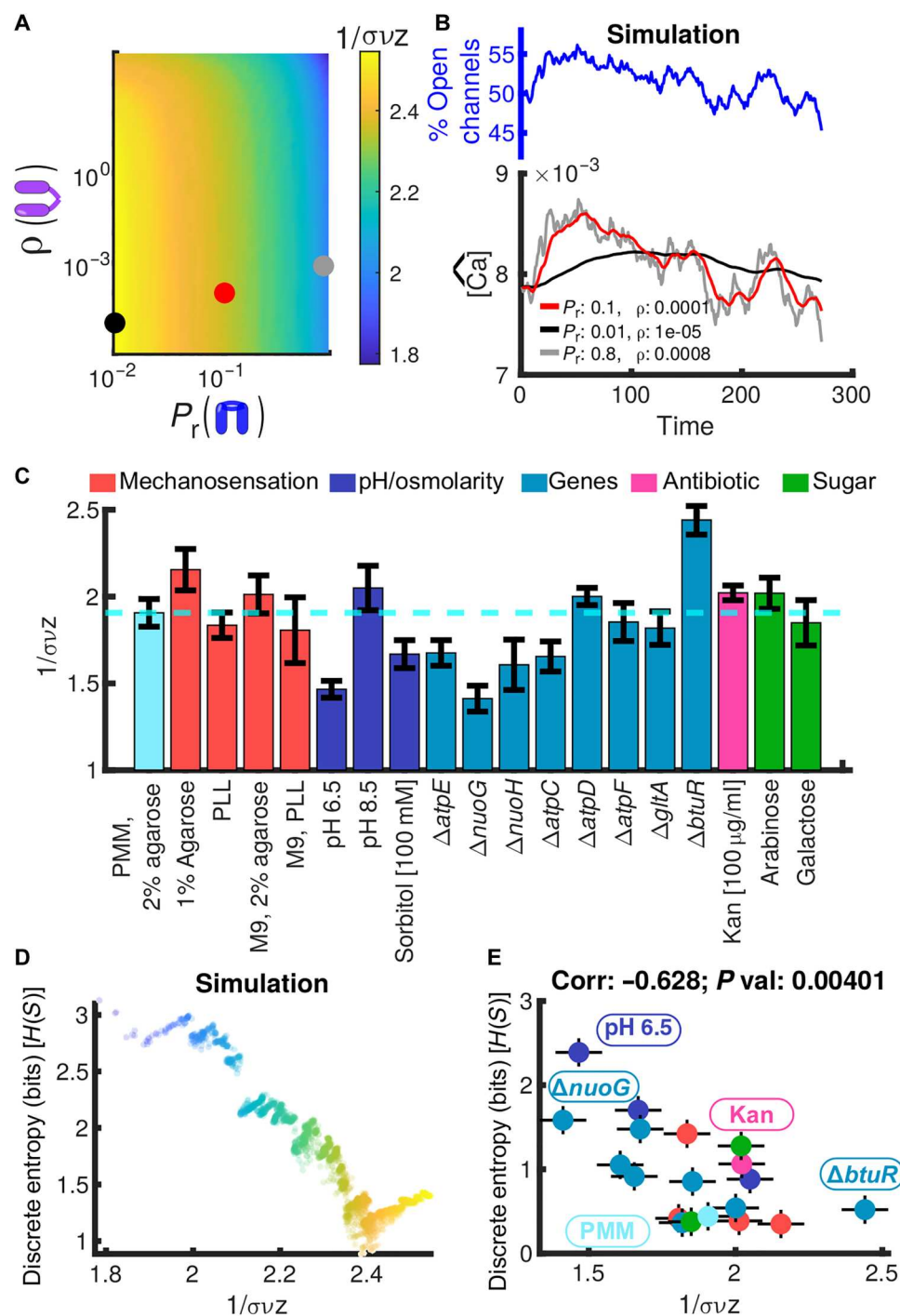


Fig. 5. Environmental and genetic factors tune the critical exponent and information capacity of bacterial populations. (A) Heatmap of the model's critical exponent (colormap), as a function of P_r (x axis) and ρ (y axis). Parameter set for Fig. 3 marked with a red dot. Black and gray dots mark simulations parameter set in (B). The critical exponent was measured using the mean size scaling estimation. (B) Simulation traces for three parameter sets. The top depicts the percentage of open channels over time (Σ) when simulating a critical network. The bottom shows the resulting Ca^{2+} dynamics for the specified P_r and ρ (legend). (C) Bar plot of critical exponent measured in labeled conditions. Standard PMM media with 2% agarose condition in cyan. Each condition was imaged at 5 Hz. (D) Simulation-based prediction of the avalanche size's discrete entropy [$H(S)$] as a function of the critical exponent ($1/\sigma vZ$). Points colored to correspond to colormap in (A). (E) Experimental correlation between $1/\sigma vZ$ and discrete $H(S)$. One hundred uniform bins were used for calculating $H(S)$ (see Materials and Methods). Error bars in (C) and (E) represent 1 SD estimated from 100 bootstrap-resampled avalanches from three replicates.

exponent, while a knockout in the catalytic site ($\Delta atpD$), which biases the pump to run in reverse generating ATP, increased the exponent (Fig. 5C, teal bars). Kanamycin treatment, previously shown to cause elevated ATP levels by inhibiting ribosome consumption of ATP (36), also increased the exponent (Fig. 5C, pink bar). The mean avalanche scaling and shape collapse estimates produced well-correlated measurements of the critical exponent across the tested conditions (fig. S13, A and B; Pearson correlation: 0.84, $P < 1 \times 10^{-5}$).

Previous studies have demonstrated that systems poised at criticality maximize their information capacity (16, 37–39). Therefore, we wondered how the observed changes in the critical exponent would alter the collective information capacity of the bacterial population. We used discrete Shannon entropy (H , Box1) to measure the information capacity of the Ca^{2+} fluctuations based on the avalanche sizes (S). The model predicted a negative correlation between entropy [$H(S)$] and the critical exponent ($1/\sigma_vz$) (Fig. 5D). When we examined $H(S)$ in the experimental data across the different conditions, we found a statistically significant negative correlation (Fig. 5E; Pearson correlation: -0.628 , $P < 1 \times 10^{-2}$) which did not depend on the bin size used to calculate discrete $H(S)$ (fig. S13C). The entropy of the system sets the upper bound on its information transmission capacity [i.e., $MI(X,Y) = H(X) - H(X|Y)$ where MI is the mutual information]; therefore, we concluded that tuning the environment and genetics changes the collective computational capacity within a population of single cells (40). Overall, this means that the diversity of environmental inputs a population of bacteria can reliably distinguish (i.e., the information capacity) depends on both their environment and genetics.

Cell autonomous diversification in the transition between motile and sessile growth driven by SOC-governed Ca^{2+} fluctuations

During our investigations, we observed mechanically stimulated cells (i.e., cells under agarose imaging pads) treated with CCCP stopped growing, despite remaining viable (fig. S11). We previously observed that mechanical stimulation drives fluctuations in Ca^{2+} and voltage and that these fluctuations were absent in cells in suspension (6). This led us to wonder whether disrupting SOC modified the cellular response to mechanosensation.

To test the influence of SOC in mechanosensation, we first compared the growth rate of cells in suspension to cells under an agarose pad for a range of CCCP concentrations. We found that cells under mechanical stimulation were more sensitive to the loss of membrane voltage by CCCP treatment (Fig. 6A) although we note that the difference was small in terms of concentration due to the high Hill slope of the dose-response curves. Growth, both under the pad and in suspension, was measured on the same day with the same cultures and drug stocks to minimize the potential for artifacts (see Materials and Methods).

We next wondered what mechanically induced signals could account for the differential CCCP growth defect. Numerous studies have identified cyclic-di-guanosine 3',5'-monophosphate (c-di-GMP) as a universal, secondary messenger governing the transition from motile to sessile growth (Table 1) including cell cycle progression under mechanical stimulation (41–43). A recent study found that c-di-GMP pools increase within minutes of cells adhering to a solid substrate (44). To measure how c-di-GMP pools depend on mechanically induced Ca^{2+} fluctuations, we used the recently developed fluorescence resonance energy transfer

(FRET) sensor TealSpy (Table 1) (45). A FRET sensor with a mutation in the c-di-GMP binding domain, NBSpy, was used as a negative control. As expected, there was no increase in the FRET signal in the NBSpy containing cells during mechanical stimulation (Fig. 6B). In contrast, we saw a persistent increase in c-di-GMP with the TealSpy construct during mechanical stimulation (Fig. 6C). When treated with CCCP, the cells did not increase c-di-GMP over time (Fig. 6D). This suggested that Ca^{2+} and/or voltage fluctuations are necessary to increase c-di-GMP pools upon mechanosensation.

Given that c-di-GMP is required for growth under mechanical stimulation, we hypothesized that increasing c-di-GMP pools would overcome the differential CCCP growth defects. The c-di-GMP levels are regulated by phosphodiesterases (PDEs; Table 1) that decrease c-di-GMP pools via hydrolysis. To ectopically increase c-di-GMP pools, we used a genetic knockout of *pdeH*, the primary PDE in *E. coli* (46). The $\Delta pdeH$ cells showed an increase in basal c-di-GMP levels (Figs. 6E and fig. S14B) and substantially faster growth under mechanical stimulation (fig. S14C) as expected. The knockout erased the mechanosensitive-specific growth defects of CCCP (Fig. 6F).

Ca^{2+} and c-di-GMP were previously connected in three independent biochemical studies that discovered metal-selective PDEs in diverse species (47–49). For all three species, the c-di-GMP PDEs were inhibited in vitro by Ca^{2+} . On the basis of this biochemical data and our data showing SOC-governed Ca^{2+} fluctuations are scale free, we predicted a high variability in c-di-GMP pools and growth rates in wild-type (WT) cells compared to $\Delta pdeH$ cells which bypass the Ca^{2+} -regulated c-di-GMP degradation. Comparing the distribution of the integrated c-di-GMP over 2 hours of mechanical stimulation showed that the untreated cells had a wide distribution of c-di-GMP with a long tail, while the CCCP cells were uniformly low (Fig. 6F, green versus yellow). Conversely, the $\Delta pdeH$ showed high c-di-GMP, suggesting that these cells bypassed the Ca^{2+} -dependent PDE inhibition (Fig. 6G, purple). The medians of these distributions were found to be statistically different using a Kruskal-Wallis test. The long tail in the SOC-intact cells suggested a high variability in commitment to growth under mechanical stimulation. The percentage of nongrowing cells under mechanical stimulation was substantially higher in WT cells as compared to the $\Delta pdeH$ cells (Fig. 6H and fig. S14, D and E). (Note: CCCP could not function as a negative control when measuring commitment to growth as the concentrations required to abrogate SOC also eliminated cell growth.) Because of the variability in commitment to sessile growth, we saw a corresponding increase in variability of microcolony sizes over time (Fig. 6, I to K). At every time point, the coefficient of variation of the colony size was significantly larger in the WT compared to the *pdeH* knockout (Fig. 6I). From the time cells that were mechanically stimulated, the WT cells had both the largest and smallest colonies (Fig. 6, J and K) despite a slower population-level growth rate (fig. S14C). In total, our data support a mechanism whereby stochastic, scale-free fluctuations in Ca^{2+} , stimulated by mechanically-induced voltage fluctuations and governed by SOC, inhibit a metal-sensitive PDE to increase the intracellular c-di-GMP pool variably across the population (Fig. 6L).

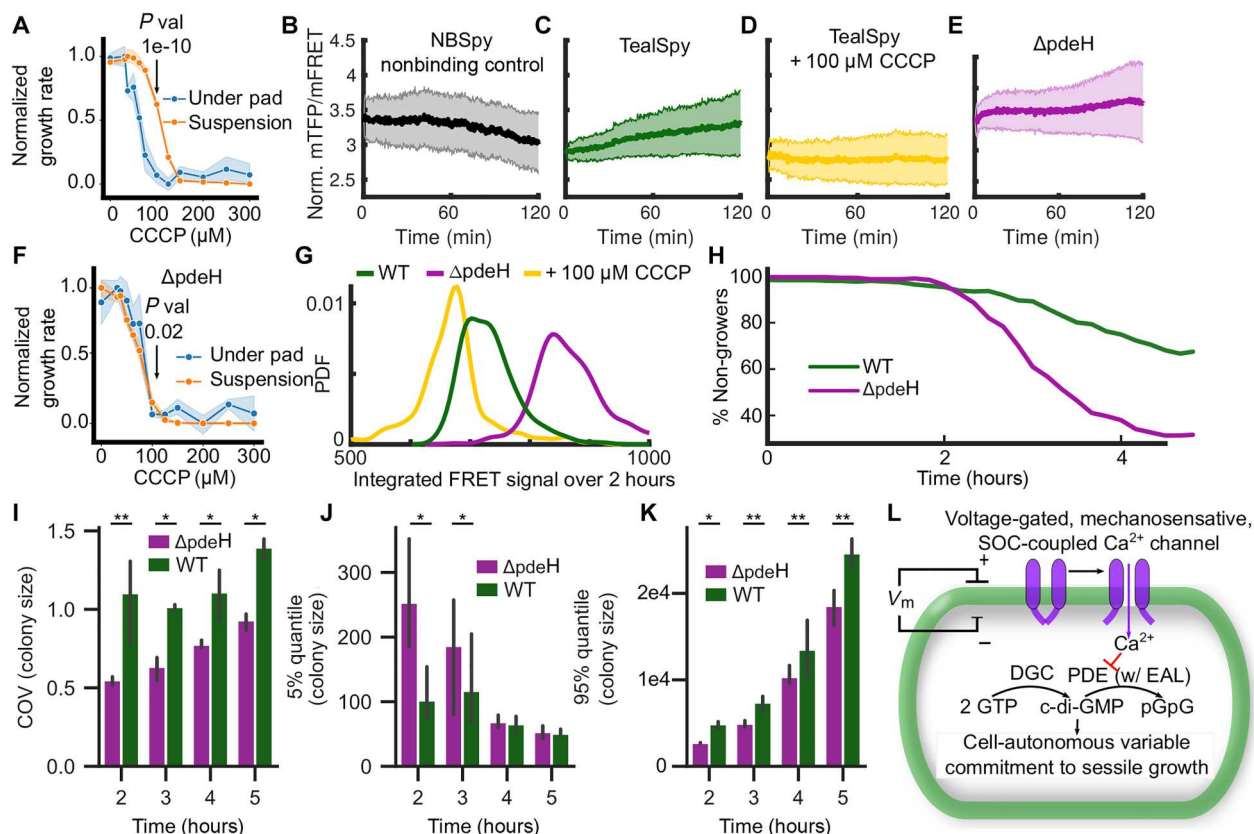


Fig. 6. SOC-governed, Ca^{2+} -regulated c-di-GMP pools diversify commitment to sessile growth. (A) Normalized growth rate during mechanical stimulation (blue) compared to motile growth (orange) as a function of CCCP concentration. P value of 100 μM CCCP condition calculated using two-tailed t test, five replicates for under pad samples and four replicates for suspension samples. (B to E) Depicted are the mean (solid line) and SD (error bars) of single-cell FRET measurements as a function of time under mechanical stimulation for the NBSpy (B), TealSpy (C), CCCP treated (D), and ΔpdeH strain (E). TealSpy is a c-di-GMP FRET sensor. NBSpy is TealSpy with a mutation in the c-di-GMP-binding *ygcR* motif. SD computed between 878, 263, 324, and 318 total cells from three replicates for (B) to (E), respectively. (F) Dose-response of ΔpdeH knockout to CCCP treatment in the motile and sessile growth phases. P value of 100 μM CCCP condition calculated using two-tailed t test, five replicates for under pad samples and four replicates for suspension samples. (G) Distribution of integrated c-di-GMP in single cells after 2 hours of growth under mechanical stimulation. Medians of distributions are significantly different (Kruskal-Wallis test, $\chi^2 = 637$, $P < 10^{-10}$). Numbers of cells analyzed for the WT, ΔpdeH , and CCCP conditions were 263, 318, and 324, respectively. (H) Percentage of non-growers over time in the WT and the ΔpdeH samples. Non-growers are defined as cells that have not exceeded $4\times$ the area of the average single cell. Between 300 and 450 colonies were counted at every time point for both conditions. (I to K) Comparing the coefficient of variation (COV) (I), 5th percentile (J), and 95th percentile (K) in colony size over time between the ΔpdeH and WT strains. $*P < 0.05$ and $**P < 0.005$ (one-tail, t test, three replicates). (L) Model of SOC-governed, cell-autonomous, commitment to sessile growth via Ca^{2+} -regulated c-di-GMP production.

DISCUSSION

The dynamic nature of bacterial electrophysiology and its role in biofilm growth and maintenance has become increasingly clear over the last decade (3, 4, 50). *B. subtilis* communicates metabolic needs electrically through a biofilm (51, 52), and these communications are governed by percolation theory (53, 54), demonstrating that single-cell organisms can co-opt physical principles which increase their collective fitness. Here, we find another elegant example of the complexity of a bacterium using the physics of SOC to regulate Ca^{2+} flux. By selecting for ion channels with the biophysical characteristics necessary to establish SOC, single-cell organisms have co-opted the physics of phase transitions for biological sensing. Our observation of SOC governing Ca^{2+} dynamics is not merely a phenomenological parallel to criticality but, in a deep statistical sense, a true phase transition (55) defined by the coupling strength between channels. Mechanisms that have evolved to homeostatically tune the strength of the Ca^{2+} channel coupling remain to

be elucidated. However, the evolutionary advantages of SOC are readily apparent. The dynamics span several orders of magnitude while simultaneously maintaining long-term stability in the face of diverse, rapidly changing environments (25, 26). Our work suggests an additional evolutionary advantage of SOC: emergent diversification of individual actors even in the absence of communication. Leveraging the stochasticity inherent at the boundary between phases, bacteria can coordinate a variable commitment to sessile growth versus the maintenance of a motile lifestyle in unpredictable environments. Prior work has shown power-law-like residence times of single-cell attachment dynamics in *Pseudomonas aeruginosa* (56). Our work points to the potential role of scale-free, mechanically stimulated fluctuations in Ca^{2+} in a bacterium's decision to invest in a sessile lifestyle. Additional investigation is necessary to determine how unique this phenomenon is to Ca^{2+} as compared with other ions such as K^+ or Na^+ , as well as how

fluctuations influence other Ca^{2+} -regulated elements of cell physiology beyond c-di-GMP (2, 3).

In addition, we found that SOC is maintained across environmental conditions; however, the critical exponent can vary. Thus, the critical exponent is not unique but exists on a continuum depending on the internal and external environments. We discovered moving along the continuum changed the collective information capacity of the population (i.e., its entropy) as increasing the critical exponent leads to decreasing the entropy in the avalanche size up to a threshold. This relationship suggests an overarching lens through which to re-examine how critical exponents and information capacity are modified in diverse SOC systems.

Limitations of study

The primary limitation of this study is the inability to directly manipulate cytosolic Ca^{2+} in *E. coli* using reagents such as bis-aminophenoxy-ethane-tetraacetic acid-acetoxy-methylester (BAPTA-AM) due to limited uptake across the double membrane. Because the flux in cytosolic Ca^{2+} originates from the periplasm in Gram-negative rods like *E. coli*, the cells are robust to external changes in Ca^{2+} . In addition, the paucity of information on the identity of Ca^{2+} effectors in *E. coli* highlights the need for further discovery of the key players in regulating bacterial electrophysiology. Without the ability to directly manipulate cytosolic Ca^{2+} , much of our study depended on altering the membrane voltage and SOC via the protonophore CCCP. Last, previous attempts to measure rapid Ca^{2+} dynamics at single-cell resolution in Gram-negative species using fluorescent dyes such as Fura2-AM have proven infeasible due to no uptake. Therefore, our studies are limited by reliance on GCaMP6f.

Another limitation was the necessity of defining an avalanche construct to use existing SOC analytics. While we observed the hallmarks of SOC for two different avalanche definitions, both approaches were pursued to leverage existing SOC frameworks (31). This limitation points to the need for extensions of classic SOC analytics to continuous signals. Also, we found the SOC analytics, in particular, the power law fits of the avalanche size (S) and duration (T), to be sensitive to slight changes in the data preprocessing. As a result, the crackling noise relationship proved to be the least reliable measure of the critical exponent.

Last, there are several areas for future improvement in our approach to model bacterial SOC. The communication between channels in our model cannot be derived from biophysical measurements but rather is patterned on the discrete, Ising-like models developed to model SOC in neural systems. As is the case in our study, the binarization of a neuron and nonthermodynamic equilibrium of these models substantially reduces their biological "realism"; nevertheless, these models have proven useful in predicting responses of neural systems to perturbations (29). Similarly, our model predicted the relationship of the entropy as a function of the critical exponent (Fig. 5, D and E) as well as the salient features observed in the GCaMP6f traces including the scale-free power spectra, branching function, and ACF (Table 2) despite this limitation. In particular, the prediction of the relationship between the critical exponent and entropy of the avalanche sizes depended on connecting the Ising-like model developed for neuroscience with the Hodgkin-Huxley model of ion flux thereby revealing a continuum of critical attractors.

MATERIALS AND METHODS

Strains and experimental configuration

E. coli strain BW25113 was acquired from the Yale Coli Genetic Stock Center, *B. subtilis* strain W168 was acquired from E. Garner (Harvard University), and *P. putida* strain KT2440 was acquired from M. Jewell. The GCaMP6f-mScarlet plasmid (Addgene #158979) was transformed into the *E. coli* and *P. putida* cells as previously described (36). GCaMP6f expression in *B. subtilis* was genetically incorporated under the hyperspank promoter with spectinomycin resistance. c-di-GMP was measured using the TealSpy FRET sensor shared by E. Petersen (45). TealSpy uses an mTFP/mKO.2 pair joined by a linker containing a conserved c-di-GMP binding domain (ycgR-based) (45). When the linker binds c-di-GMP, the fluorophore undergoes a conformational shift activating FRET. The optimal concentration of arabinose (0.001%) was determined by growth rate at 30°C as a function of arabinose concentration (fig. S14A). Bacteria were grown overnight in LB medium and diluted 1:50 from overnight cultures into PMM except for the TealSpy and NBSpy constructs which were diluted 1:8. After 2 hours of outgrowth, cells were immobilized onto agarose pads for imaging (57). The cephalixin experiment was based on the protocol for forming spheroplasts (58) without stripping the outer membrane. See the Supplementary Materials for details on pad preparation, imaging configuration, and different environmental conditions. Genetic knockout strains were selected from the Keio library expressing GCaMP6f (33). We note that the identity of the voltage-gated Ca^{2+} channel(s) in *E. coli* remains unknown despite a genome-wide, functional genomic screen.

For the growth assays with CCCP, all the suspension and under pad growth conditions at different concentrations of CCCP were tested on the same day with the same drug dilution. This was necessitated by the high hill slope of CCCP. CCCP 1M stock was diluted to 100× before running the dilution series in dimethyl sulfoxide. The dilution series (12 doses) was added to six replicates of preculture cells shaken for 2 hours before treatment. After shaking for an additional hour, the 2 μl of the cells was plated on agarose pads with matching CCCP concentrations. The growth in the plates was measured by optical density using a plate reader (Techan Spark) with environmental controls (30°C) in a flat-bottomed 96-well plate (100 μl of cells in each well). Measurements were taken every 2.5 min with shaking in between. Plates were parafilm-wrapped and incubated in a humidity cassette to minimize edge evaporation. For the conditions under the pad, the percentage of pixels in the image with an intensity above a static threshold was used to measure the area of the field of view comprised by cells. Growth rates were calculated by fitting an exponential growth model to both datasets. Normalization to the untreated control was used to visualize the different dose-responses for suspension and mechanically stimulated cells.

Image processing

Image processing was done using custom scripts written in MATLAB (MathWorks, R2020a) and followed the general scheme described in (36, 57). Following illumination correction, jitter correction, and local background subtraction, cells were segmented using a Hessian-based algorithm (*fibermetric*) in MATLAB specific for identifying tubular structures. For each segmented object, the mean fluorescent signal over time was extracted. This constituted

the cell's "trace" (Table 1). Subsequently, the global background was subtracted from the trace. To remove rare, segmented debris, a multidimensional gating approach based on morphological features of segmented objects was used as in (57).

For all signals, we removed the first 15 frames of imaging to account for initial photobleaching. In instances where the loss of signal was substantial, including the mScarlet signal and GCaMP6f imaging in *B. subtilis*, an additional correction was applied by fitting an exponential equation of the form $a_1 * e^{-b_1 t} + a_2 * e^{-b_2 t} + c$ to each trace and dividing the trace by the equation fit.

To calculate the FRET signal for the c-di-GMP sensors, the FRET signal (light passing emission filter 568LP when exciting at 440 nm) and the mTFP signal (light passing emission filter 535/20 when exciting at 440 nm) were both normalized independently per cell, and then the ratio mTFP/mFRET over time was divided by the normalized ratio at the first time point and multiplied by the mean nonnormalized FRET ratio to retain the correct magnitude. Additional details are provided in the Supplementary Materials.

Analysis

To normalize the power spectra, a time step of 1 was assigned to all frequencies, and the mean-centered traces were normalized individually using z-score normalization. Fitting the power spectra to the power law ($|P(f)| \sim f^{-x}$) and exponential ($|P(f)| \sim e^{-x}$) functions was done using linear regression in log-transformed space to weight correctly fitting the tail. The flicker noise ($|P(f)| \sim D/(f+k)$) function was fit using a nonlinear least squares optimizer in a log-transformed space. AIC calculations were done including the correction factor for small sample sizes (59). If the different imaging frequencies could not be well fit when combined, then each frequency was fit independently. The ACF was calculated using the cross-correlation function (*xcorr*) in MATLAB for all traces.

To calculate the fractal dimension of the GCaMP6f traces, we measured the Hurst exponent (*h*) computed with the adaptive fractal algorithm (AFA) (fig. S3, A to D) (60). *h* is a measure of long-term memory in a time series and is related to the fractal dimension (*D*) by $D = 2 - h$ for a one-dimensional time series (61). As the power spectra exponents are <1 (Fig. 1E), Ca^{2+} transients are a stationary, long-memory process (fractional Gaussian motion). Integrating the signal results in the fractional Brownian motion from which we calculate the Hurst exponent (*h*) AFA (62, 63) using a custom MATLAB implementation (fig. S3, A to D). When imaging at 5 Hz, we found it necessary to correct for photobleaching before calculating the Hurst exponent to avoid trivially identifying autocorrelated traces due to a modest decrease in signal over time. All imaging frequencies have 215 frames used to calculate *h*. The Hurst exponent was not calculated for mScarlet or fluorescein as they do not satisfy the required properties for Hurst analysis, namely, the presence of power-law distributed power spectra (60). See Supplementary Methods for additional details.

Branching analysis was done according to (27). The branching term Λ was calculated by dividing the GCaMP6f signal at $f+1$ by the signal at f for all cells at all time points. According to theory, the Λ value should be near 1 in the critical region dropping below one for high values of Ca^{2+} and increasing above one for low values of Ca^{2+} (Fig. 2, A and B). This is a result of the system being driven back toward equilibrium proportional to the distance from the critical region. To compare the branching ratio between different signals, we z-score normalized the mScarlet, fluorescein, and

GCaMP6f signals for both WT and heat-killed controls before calculating the branching ratio.

For calculating the critical exponent $1/\sigma_{\text{vz}}$, we used three approaches as recommended for identifying SOC systems (13, 30, 31).

First, the mean size of the avalanche for a given duration [$\langle S \rangle(T)$] should be proportional to the duration (*T*) scaled by $1/\sigma_{\text{vz}}$.

$$\langle S \rangle(T) \sim T^{1/\sigma_{\text{vz}}} \quad (1)$$

Second, the integrated size *S* and duration *T* of avalanches should both be power-law distributed with exponents τ and α , respectively, and relate to $1/\sigma_{\text{vz}}$ by their ratio as follows

$$P(S) \sim S^{-\tau}; P(T) \sim T^{-\alpha}; 1/\sigma_{\text{vz}} = (\alpha - 1)/(\tau - 1) \quad (2)$$

Last, the renormalized, mean shape of the avalanche for each avalanche duration [$s(t, T)$] scaled by $T^{1-1/\sigma_{\text{vz}}}$ should collapse for all periods *T*. Explicitly

$$s(t, T) * T^{1-1/\sigma_{\text{vz}}} \sim F(t, T) \quad (3)$$

where $F(t, T)$ is the renormalized avalanche duration. This relationship, based on renormalization group theory derived for ferromagnets (64), is commonly termed shape collapse (31).

Power-law probability distribution fitting for size and duration of avalanches based on MLE was done using code from A. Clauset (32) available from <https://aaronclauset.github.io/powerlaws/>. This code implements a lattice search algorithm to find the minimum cutoff for truncated power-law fits. The likelihood (*P* value) of power-law distribution was calculated using the KS test algorithm approach proposed by A. Clauset. When the *P* value is greater than 0.01, the null hypothesis that the data come from a power-law distribution cannot be rejected. Fitting critical exponent $1/\sigma_{\text{vz}}$ from the mean avalanche scaling (Eq. 1) was done using standard linear regression. The mean avalanche size for a given period was calculated before taking the log transform. The algorithm for estimating the critical exponent from the avalanche shape collapse is based on minimizing the distance between the rescaled mean avalanche shapes for each period (31). For both the mean avalanche scaling and the shape collapse estimates, avalanche durations with less than 10 instances were removed to reliably calculate the mean size and shape. Additional algorithm details for calculating $1/\sigma_{\text{vz}}$ are in the Supplementary Materials.

The diffusion rates for ATP, Ca^{2+} , and H^+ are $3.54 \times 10^{-6} \text{ cm}^2/\text{s}$ (65), $5.3 \times 10^{-6} \text{ cm}^2/\text{s}$ (66), and $605 \times 10^{-7} \text{ cm}^2/\text{s}$ (67), respectively. These lengths were used to calculate the average displacement as a function of time according to Fick's second law $\sqrt{(2 * D * d * t)}$ where *D* is the diffusion rate, *d* is the dimension, and *t* is the time. Since we were interested in the diffusion rate along the axis of the cell body, we set *d* = 1. The mean displacement for ATP, Ca^{2+} , and H^+ in 5 ms was calculated to be 1.8, 2.3, and 7.8 μm , respectively.

Shannon entropy for avalanche sizes was calculated by $H(S) = -\sum_{j=1}^{100} p(S_j) \log_2[p(S_j)]$ where $p(S)$ is the probability of an avalanche of size *S*. The probability was estimated by uniformly binning all the avalanches into 100 bins for all conditions; however, the observed negative correlation was invariant to the number of bins used (fig. S13C).

All code required to generate the figures is available from https://bitbucket.org/meyerct6/soc_bacteria_repo/src/master/. In addition,

the compiled experimental database, in an HDF5 format, with all the single-cell fluorescent traces for all conditions is available from the same. See the Supplementary Materials for details on the database organization.

Modeling

To model the Ca^{2+} current, we make several simplifying assumptions. First, we assume the Ca^{2+} current is the sum of Ca^{2+} influx due to passive electrodiffusion through Ca^{2+} channels (Fig. 3A, purple) and efflux by way of Ca^{2+} pumps (Fig. 3A, blue). The rate of pumping (P_r) is proportional to the distance from some set point (ϵ_2). The rate of electrodiffusion is specified by Ohm's law and is equal to the difference between the reversal voltage (i.e., Nernst potential) and the membrane voltage (V_m) multiplied by the membrane conductance. The constants in the voltage difference can be grouped into the term ϵ_1 . We define conductance to be the product of the maximal conductance (ρ) times the percent of open channels (Σ) analogous to the Hodgkin and Huxley formulation for a neuron. We also assume that the external calcium ($\text{Ca}_{\text{out}}^{2+}$) is a large static reservoir and V_m is a constant. The validity of this assumption was checked on the basis of estimates of the periplasmic and cytosolic concentrations of Ca^{2+} from the Campbell lab (5). They found that the periplasmic concentration is >0.1 mM in rough equilibrium with the media concentration, while the cytoplasmic concentration ranged between 300 nM and 1 μM . On the basis of the conservative estimate that the periplasm takes up at least 20% of the total cell volume (68), we would expect there to be approximately ~ 240 Ca^{2+} ions in the cytosol (500 nM) and 12,044 (0.1 mM) ions in the periplasm of a 1 femtoliter bacterium corresponding to $50\times$ difference. Therefore, the approximation of a much larger reservoir which is not depleted is valid.

Last, we write our ODE in terms of the normalized internal calcium $\hat{\text{Ca}}^{2+} = \frac{\text{Ca}_{\text{in}}^{2+}}{\text{Ca}_{\text{out}}^{2+}}$. The resulting ODE is

$$\dot{\phi} = [-\ln(\hat{\text{Ca}}^{2+}) - \epsilon_1] \rho \sum -(\hat{\text{Ca}}^{2+} - \epsilon_2) P_r$$

See the Supplementary Materials for full derivation.

We note that, because of calcium's charge, Φ measures the change in the internal concentration. As $\text{Ca}_{\text{in}}^{2+} < \text{Ca}_{\text{out}}^{2+}$, $\log(\hat{\text{Ca}}^{2+}) < 0$ and $\epsilon_1 < 0$ as $V_m < 0$; therefore, the influx due to electrodiffusion is always positive. In addition, as $\hat{\text{Ca}}^{2+} > \epsilon_2$, the efflux via the pump is always negative.

The model was simulated in one of two ways. First, to simulate uncoupled channels, the probability of opening a channel at any time step was 50% regardless of the state of all other channels. To couple the channels, we defined a directed network (Fig. 3B) such that the odds of opening a channel depend on the weighted input of all other channels' current state. The edge weights in this network define a matrix A (Fig. 3B), and the state of the network nodes (S) after 1 time step can be determined as $s(t+1) = A \cdot s(t) > R$ where R is a random number generated over a uniform distribution on the interval $[0,1]$. We draw our matrix weights $[A(i,j)]$ from an exponential distribution (fig. S9A). Previous studies have shown the long-term system dynamics are determined by the maximum eigenvalue (λ) of the matrix and when $\lambda = 1$ critical dynamics emerge (27, 34, 35). To define a specific λ value, we set the mean of exponential distribution equal to one divided by the number of channels (i.e., the number of matrix rows/columns). According to the Perron-Frobenius theorem, the maximum eigenvalue (Table 1) is bounded

between the minimum and maximum sum of all the columns (fig. S9D). However, the bounds are proportional to the number of channels in the model necessitating large numbers of channels ($>10^3$) to prevent simulations from collapsing (fig. S9, C and E). Therefore, we use 10^4 channels in our simulations.

Supplementary Materials

This PDF file includes:

Supplemental Methods

Figs. S1 to S14

Legends for movies S1 and S2

Other Supplementary Material for this manuscript includes the following:

Movies S1 and S2

REFERENCES AND NOTES

1. L. Galera-Laporta, C. J. Comerici, J. Garcia-Ojalvo, G. M. Süel, IonoBiology: The functional dynamics of the intracellular metallome, with lessons from bacteria. *Cell Syst.* **12**, 497–508 (2021).
2. D. C. Dominguez, Calcium signaling in prokaryotes, in *Calcium and Signal Transduction* (InTech, 2018).
3. J. M. Benarroch, M. Asally, The microbiologist's guide to membrane potential dynamics. *Trends Microbiol.* **28**, 304–314 (2020).
4. J. M. Kralj, D. R. Hochbaum, A. D. Douglass, A. E. Cohen, Electrical spiking in *Escherichia coli* probed with a fluorescent voltage-indicating protein. *Science* **333**, 345–348 (2011).
5. H. E. Jones, I. B. Holland, A. K. Campbell, Direct measurement of free Ca^{2+} shows different regulation of Ca^{2+} between the periplasm and the cytosol of *Escherichia coli*. *Cell Calcium* **32**, 183–192 (2002).
6. G. N. Bruni, R. A. Weekley, B. J. T. Dodd, J. M. Kralj, Voltage-gated calcium flux mediates *Escherichia coli* mechanosensation. *Proc. Natl. Acad. Sci. U.S.A.* **114**, 9445–9450 (2017).
7. M. M. King, B. B. Kayastha, M. J. Franklin, M. A. Patrauchan, Calcium regulation of bacterial virulence, in *Advances in Experimental Medicine and Biology* (Springer, 2020), vol. 1131, pp. 827–855.
8. P. Bak, C. Tang, K. Wiesenfeld, Self-organized criticality: An explanation of the $1/f$ noise. *Phys. Rev. Lett.* **59**, 381–384 (1987).
9. J. P. Sethna, K. A. Dahmen, C. R. Myers, Crackling noise. *Nature* **410**, 242–250 (2001).
10. W. Bialek, A. Cavagna, I. Giardinà, T. Mora, E. Silvestri, M. Viale, A. M. Walczak, Statistical mechanics for natural flocks of birds. *Proc. Natl. Acad. Sci. U.S.A.* **109**, 4786–4791 (2012).
11. J. Hesse, T. Gross, Self-organized criticality as a fundamental property of neural systems. *Front. Syst. Neurosci.* **8**, 166 (2014).
12. S. Helmrich, A. Arias, G. Lochead, T. M. Wintermantel, M. Buchhold, S. Diehl, S. Whitlock, Signatures of self-organized criticality in an ultracold atomic gas. *Nature* **577**, 481–486 (2020).
13. J. B. Mallinson, S. Shirai, S. K. Acharya, S. K. Bose, E. Galli, S. A. Brown, Avalanches and criticality in self-organized nanoscale networks. *Sci. Adv.* **5**, eaaw8438 (2019).
14. J. M. Beggs, D. Plenz, Neuronal avalanches in neocortical circuits. *J. Neurosci.* **23**, 11167–11177 (2003).
15. P. (Per) Bak, *How Nature Works: The Science of Self-Organized Criticality* (Copernicus, 1999).
16. W. L. Shew, H. Yang, S. Yu, R. Roy, D. Plenz, Information capacity and transmission are maximized in balanced cortical networks with neuronal avalanches. *J. Neurosci.* **31**, 55–63 (2011).
17. M. A. Muñoz, Colloquium: Criticality and dynamical scaling in living systems. *Rev. Mod. Phys.* **90**, 031001 (2018).
18. T.-W. Chen, T. J. Wardill, Y. Sun, S. R. Pulver, S. L. Renninger, A. Baohian, E. R. Schreiter, R. A. Kerr, M. B. Orger, V. Jayaraman, L. L. Looger, K. Svoboda, D. S. Kim, Ultrasensitive fluorescent proteins for imaging neuronal activity. *Nature* **499**, 295–300 (2013).
19. B. D. Malamud, G. Morein, D. L. Turcotte, Forest fires: An example of self-organized critical behavior. *Science* **281**, 1840–1842 (1998).
20. C. J. Rhodes, R. M. Anderson, Power laws governing epidemics in isolated populations. *Nature* **381**, 600–602 (1996).
21. F. N. Hooge, $1/f$ noise sources. *IEEE Trans. Electron Devices* **41**, 1926–1935 (1994).
22. M. B. Elowitz, A. J. Levine, E. D. Siggia, P. S. Swain, Stochastic gene expression in a single cell. *Science* **297**, 1183–1186 (2002).
23. C. E. Rasmussen, C. K. I. Williams, *Gaussian Processes for Machine Learning* (MIT Press, 2005).

24. S. Karlin, H. M. Taylor, *A Second Course in Stochastic Processes* (1981).
25. G. Werner, Fractals in the nervous system: Conceptual implications for theoretical neuroscience. *Front. Physiol.* **1**, 15 (2010).
26. W. L. Shew, D. Plenz, The functional benefits of criticality in the cortex. *Neuroscientist* **19**, 88–100 (2013).
27. D. B. Larremore, W. L. Shew, E. Ott, F. Sorrentino, J. G. Restrepo, Inhibition causes ceaseless dynamics in networks of excitable nodes. *Phys. Rev. Lett.* **112**, 138103 (2014).
28. E. Schneidman, M. J. Berry, R. Segev, W. Bialek, Weak pairwise correlations imply strongly correlated network states in a neural population. *Nature* **440**, 1007–1012 (2006).
29. Z. Ma, G. G. Turrigiano, R. Wessel, K. B. Hengen, Cortical circuit dynamics are homeostatically tuned to criticality in vivo. *Neuron* **104**, 655–664.e4 (2019).
30. J. Touboul, A. Destexhe, Power-law statistics and universal scaling in the absence of criticality. *Phys. Rev. E* **95**, 012413 (2017).
31. N. Marshall, N. M. Timme, N. Bennett, M. Ripp, E. Lautzenhiser, J. M. Beggs, Analysis of power laws, shape collapses, and neural complexity: New techniques and MATLAB support via the NCC Toolbox. *Front. Physiol.* **7**, 250 (2016).
32. A. Clauset, C. R. Shalizi, M. E. J. Newman, Power-law distributions in empirical data. *SIAM Rev.* **51**, 661–703 (2009).
33. R. Luder, G. N. Bruni, J. M. Kralj, Genome-wide functional screen for calcium transients in *Escherichia coli* identifies increased membrane potential adaptation to persistent DNA damage. *J. Bacteriol.* **203**, e00509-20 (2021).
34. D. B. Larremore, M. Y. Carpenter, E. Ott, J. G. Restrepo, Statistical properties of avalanches in networks. *Phys. Rev. E* **85**, 066131 (2012).
35. S. Pei, S. Tang, S. Yan, S. Jiang, X. Zhang, Z. Zheng, How to enhance the dynamic range of excitatory-inhibitory excitable networks. *Phys. Rev. E* **86**, 021909 (2012).
36. G. N. Bruni, J. M. Kralj, Membrane voltage dysregulation driven by metabolic dysfunction underlies bactericidal activity of aminoglycosides. *eLife* **9**, e58706 (2020).
37. S. A. Kauffman, Emergent properties in random complex automata. *Physica D* **10**, 145–156 (1984).
38. W. Maass, T. Natschläger, H. Markram, Real-time computing without stable states: A new framework for neural computation based on perturbations. *Neural Comput.* **14**, 2531–2560 (2002).
39. N. Bertschinger, T. Natschläger, Real-time computation at the edge of chaos in recurrent neural networks. *Neural Comput.* **16**, 1413–1436 (2004).
40. R. Cheong, A. Rhee, C. J. Wang, I. Nemenman, A. Levchenko, Information transduction capacity of noisy biochemical signaling networks. *Science* **334**, 354–358 (2011).
41. A. Duerig, S. Abel, M. Folcher, M. Nicollier, T. Schwede, N. Amiot, B. Giese, U. Jenal, Second messenger-mediated spatiotemporal control of protein degradation regulates bacterial cell cycle progression. *Genes Dev.* **23**, 93–104 (2009).
42. U. Römling, M. Y. Galperin, M. Gomelsky, Cyclic di-GMP: The first 25 years of a universal bacterial second messenger. *Microbiol. Mol. Biol. Rev.* **77**, 1–52 (2013).
43. U. Jenal, A. Reinders, C. Lori, Cyclic di-GMP: Second messenger extraordinaire. *Nat. Rev. Microbiol.* **15**, 271–284 (2017).
44. A. M. Vrabioiu, H. C. Berg, Signaling events that occur when cells of *Escherichia coli* encounter a glass surface. *Proc. Natl. Acad. Sci. U.S.A.* **119**, e2116830119 (2022).
45. E. Petersen, E. Mills, S. I. Miller, Cyclic-di-GMP regulation promotes survival of a slow-replicating subpopulation of intracellular *Salmonella* Typhimurium. *Proc. Natl. Acad. Sci. U.S.A.* **116**, 6335–6340 (2019).
46. A. Boehm, M. Kaiser, H. Li, C. Spangler, C. A. Kasper, M. Ackermann, V. Kaever, V. Sourjik, V. Roth, U. Jenal, second messenger-mediated adjustment of bacterial swimming velocity. *Cell* **141**, 107–116 (2010).
47. M. Christen, B. Christen, M. Folcher, A. Schuarte, U. Jenal, Identification and characterization of a cyclic di-GMP-specific phosphodiesterase and its allosteric control by GTP. *J. Biol. Chem.* **280**, 30829–30837 (2005).
48. A. J. Schmidt, D. A. Ryjenkov, M. Gomelsky, The ubiquitous protein domain EAL is a cyclic diguanylate-specific phosphodiesterase: Enzymatically active and inactive EAL domains. *J. Bacteriol.* **187**, 4774–4781 (2005).
49. R. Tamayo, A. D. Tischler, A. Camilli, The EAL domain protein VieA is a cyclic diguanylate phosphodiesterase. *J. Biol. Chem.* **280**, 33324–33330 (2005).
50. J. Liu, R. Martinez-Corral, A. Prindle, D.-Y. D. Lee, J. Larkin, M. Gabalda-Sagarra, J. Garcia-Ojalvo, G. M. Süel, Coupling between distant biofilms and emergence of nutrient time-sharing. *Science* **356**, 638–642 (2017).
51. A. Prindle, J. Liu, M. Asally, S. Ly, J. Garcia-Ojalvo, G. M. Süel, Ion channels enable electrical communication in bacterial communities. *Nature* **527**, 59–63 (2015).
52. J. Liu, A. Prindle, J. Humphries, M. Gabalda-Sagarra, M. Asally, D. D. Lee, S. Ly, J. Garcia-Ojalvo, G. M. Süel, Metabolic co-dependence gives rise to collective oscillations within biofilms. *Nature* **523**, 550–554 (2015).
53. J. W. Larkin, X. Zhai, K. Kikuchi, S. E. Redford, A. Prindle, J. Liu, S. Greenfield, A. M. Walczak, J. Garcia-Ojalvo, A. Mugler, G. M. Süel, Signal percolation within a bacterial community. *Cell Syst.* **7**, 137–145.e3 (2018).
54. X. Zhai, J. W. Larkin, K. Kikuchi, S. E. Redford, U. Roy, G. M. Süel, A. Mugler, Statistics of correlated percolation in a bacterial community. *PLOS Comput. Biol.* **15**, e1007508 (2019).
55. T. Mora, W. Bialek, Are biological systems poised at criticality? *J. Stat. Phys.* **144**, 268–302 (2011).
56. C. K. Lee, J. Vachier, J. de Anda, K. Zhao, A. E. Baker, R. R. Bennett, C. R. Armbruster, K. A. Lewis, R. L. Tarnopol, C. J. Lomba, D. A. Hogan, M. R. Parsek, G. A. O'toole, R. Golestanian, G. C. L. Wong, Social cooperativity of bacteria during reversible surface attachment in young biofilms: A quantitative comparison of *Pseudomonas aeruginosa* PA14 and PAO1. *MBio* **11**, e02644-19 (2020).
57. C. T. Meyer, M. P. Jewell, E. J. Miller, J. M. Kralj, Machine learning establishes single-cell calcium dynamics as an early indicator of antibiotic response. *Microorganisms* **9**, 1000 (2021).
58. D. M. Figueroa, H. M. Wade, K. P. Montales, D. E. Elmore, L. E. O. Darling, Production and visualization of bacterial spheroplasts and protoplasts to characterize antimicrobial peptide localization. *J. Vis. Exp.* **57904**, (2018).
59. J. E. Cavanaugh, Unifying the derivations for the Akaike and corrected Akaike information criteria. *Stat. Probab. Lett.* **33**, 201–208 (1997).
60. A. Eke, P. Hermán, J. B. Bassingthwaite, G. M. Raymond, D. B. Percival, M. Cannon, I. Balla, C. Ikrényi, Physiological time series: Distinguishing fractal noises from motions. *Pflügers Arch.* **439**, 403–415 (2000).
61. B. B. Mandelbrot, Self-affine fractals and fractal dimension. *Phys. Scr.* **32**, 257–260 (1985).
62. I. Pilgrim, R. P. Taylor, Fractal analysis of time-series data sets: Methods and challenges, in *Fractal Analysis* (IntechOpen, 2019).
63. M. A. Riley, S. Bonnette, N. Kuznetsov, S. Wallot, J. Gao, A tutorial introduction to adaptive fractal analysis. *Front. Physiol.* **3**, 371 (2012).
64. L. P. Kadanoff, Scaling laws for ising models near T_c . *Phys. Phys. Fiz.* **2**, 263–272 (1966).
65. M. J. Hubley, R. C. Rosanske, T. S. Moerland, Diffusion coefficients of ATP and creatine phosphate in isolated muscle: Pulsed gradient ^{31}P NMR of small biological samples. *NMR Biomed.* **8**, 72–78 (1995).
66. B. S. Donahue, R. F. Abercrombie, Free diffusion coefficient of ionic calcium in cytoplasm. *Cell Calcium* **8**, 437–448 (1987).
67. P. Swietach, M. Zaniboni, A. K. Stewart, A. Rossini, K. W. Spitzer, R. D. Vaughan-Jones, Modelling intracellular H^+ ion diffusion. *Prog. Biophys. Mol. Biol.* **83**, 69–100 (2003).
68. T. M. Schmidt, Ed., *Encyclopedia of Microbiology* (Academic Press, ed. 4, 2019).

Acknowledgments: We would like to thank D. Larremore for critical insights relating to the construction of the model. We would like to thank E. Petersen for providing the TealSpy and NBSPy constructs. We would like thank A. Clauset for providing code to analyze power-law distributions. We also thank M. Jewell, E. Miller, and Z. Berriman-Rozen for helpful discussions. Last, we would like to thank E. Garner for sharing the *B. subtilis* strain and M. Jewell for sharing the *P. putida* strain expressing GCaMP6f. **Funding:** This work was supported by Searle Scholars Program and NIH New Innovator award (1DP2GM123458) to J.M.K and NIH T32 Training Grant on the Integrative Physiology of Aging (#5T32AG000279-14) and K99/R00 Pathway to Independence Award from NIAID (1K99AI175656) to C.T.M. **Author contributions:** Conceptualization: C.T.M. and J.M.K. Methodology: C.T.M. and J.M.K. Formal analysis: C.T.M. and J.M.K. Investigation: C.T.M. and J.M.K. Data curation: C.T.M. Writing—original draft preparation: C.T.M. Writing—review and editing: C.T.M. and J.M.K. Visualization: C.T.M. and J.M.K. Supervision and funding acquisition: C.T.M. and J.M.K. All authors have read and agreed to the published version of the manuscript. **Competing interests:** The authors declare that they have no competing interests. The funders had no role in the design of the study; in the collection, analyses, or interpretation of data; in the writing of the manuscript; or in the decision to publish the results. **Data and materials availability:** All processed data, compiled into an HDF5 database, are available from GitHub at the following address https://bitbucket.org/meyerct6/soc_bacteria_repo/src/master/ and are published using Zenodo (<https://doi.org/10.5281/zenodo.7893421>). All data needed to evaluate the conclusions in the paper are present in the paper and/or the Supplementary Materials. All code required to recreate figures is available from GitHub at the following address https://bitbucket.org/meyerct6/soc_bacteria_repo/src/master/ and are published under Creative Commons 4.0 International license on Zenodo (<https://doi.org/10.5281/zenodo.7893421>).

Submitted 14 December 2022

Accepted 3 July 2023

Published 4 August 2023

10.1126/sciadv.adg3028